

## QUANTUM SIMULATION

# Site-resolved imaging of a fermionic Mott insulator

Daniel Greif, Maxwell F. Parsons, Anton Mazurenko, Christie S. Chiu, Sebastian Blatt,\* Florian Huber, Geoffrey Ji, Markus Greiner†

The complexity of quantum many-body systems originates from the interplay of strong interactions, quantum statistics, and the large number of quantum-mechanical degrees of freedom. Probing these systems on a microscopic level with single-site resolution offers important insights. Here we report site-resolved imaging of two-component fermionic Mott insulators, metals, and band insulators, using ultracold atoms in a square lattice. For strong repulsive interactions, we observed two-dimensional Mott insulators containing over 400 atoms. For intermediate interactions, we observed a coexistence of phases. From comparison to theory, we find trap-averaged entropies per particle of 1.0 times the Boltzmann constant ( $k_B$ ). In the band insulator, we find local entropies as low as 0.5  $k_B$ . Access to local observables will aid the understanding of fermionic many-body systems in regimes inaccessible by modern theoretical methods.

**D**etection and control of quantum many-body systems at the level of single lattice sites and single particles gives access to correlation functions and order parameters on a microscopic level. These capabilities promise insights into a number of complex and poorly understood quantum phases, such as spin liquids, valence-bond solids, and  $d$ -wave superconductors (1, 2). Site-resolved detection and control of the wave function remain elusive in conventional solid-state systems, but are possible in synthetic matter with ultracold atoms in optical lattices, because the associated length scales are accessible with high-resolution optical microscopy (3). Site-resolved imaging of bosonic quantum gases has enabled studies of the superfluid-to-Mott insulator (MI) transition on a single-site level (4, 5), an experimental realization of Ising and Heisenberg spin chains (6, 7), a direct measurement of entanglement entropy (8), and studies of dynamics of charge and spin degrees of freedom of quantum systems (9, 10). The extension of site-resolved imaging to fermionic atoms may enable exploration of the rich phase diagram of the Hubbard model, thought to describe a variety of strongly correlated quantum-mechanical phenomena, including high-temperature superconductivity (11). Recently, site-resolved imaging of fermionic atoms has been demonstrated with different atomic species (12–15), and a single-spin band insulator has been observed (16). Although fermionic MIs and short-range antiferromagnetic spin correlations have been observed using conventional imaging techniques (17–26), site-resolved imaging of interacting many-body states of fermions is an outstanding challenge.

Here we demonstrate site-resolved observations of fermionic metals, MIs, and band insu-

lators. A fermionic MI is a prime example of a strongly interacting many-body state, where repulsive interactions between fermionic particles in two different spin states give rise to insulating behavior in a half-filled energy band. This behavior is well described by the Hubbard model. For low temperatures, a theoretical analysis of the phase diagram becomes difficult owing to the fermion sign problem (27). At temperatures above the magnetic exchange energy, spin order is absent, and a density-order crossover from a metallic state to a MI occurs when the ratio of interaction to kinetic energy is increased. Whereas the metallic state has a gapless excitation spectrum, is compressible, and shows a large variance in the site-resolved lattice occupation, the MI has a finite energy gap, is incompressible, and shows a vanishing variance in the occupation. Observing these characteristic properties of a MI requires temperatures well below the energy gap. For lower interactions and large filling, an incompressible band insulator of doublons (two particles on a site) appears because of the Pauli exclusion principle. This behavior is in contrast to the bosonic case, where the absence of the Pauli exclusion principle allows higher fillings, and a ring structure of MI states with different integer fillings appears (4, 5).

The starting point of the experiment is a low-temperature, two-dimensional gas of fermionic  $^6\text{Li}$  atoms with repulsive interactions in an equal mixture of the two lowest hyperfine ground states. After the preparation and cooling of the cloud, we set the  $s$ -wave scattering length to values  $a = 37\,a_0 - 515\,a_0$  by adjusting a magnetic bias field in the vicinity of the Feshbach resonance located at 832 G, where  $a_0$  denotes the Bohr radius (28). We then load the atoms into a square optical lattice using a 30-ms long linear ramp of the laser beam powers. The system is well described by a single-band two-dimensional Hubbard model on a square lattice with nearest-neighbor tunneling  $t_x/\hbar = 0.279(10)$  kHz and  $t_y/\hbar = 0.133(4)$  kHz along the two lattice di-

rections with a corresponding bandwidth  $8\bar{t} = 1.65(7)$  kHz and  $U/\hbar = 1.81(3)$  to  $25.2(5)$  kHz. The explored ratios of  $U/8\bar{t}$  thus range from the metallic ( $U \sim 8\bar{t}$ ) to the MI ( $U \gg 8\bar{t}$ ) regime. In the experiment, an overall harmonic confinement is present, with frequencies  $\omega_x/2\pi = 0.691(9)$  kHz and  $\omega_y/2\pi = 0.604(3)$  kHz. For more details, see (29).

We detect the many-body state of the system by measuring the occupation of each lattice site with single-site resolution. For the detection, we first rapidly increase all lattice depths to pin the atomic distribution and then image the fluorescence of the atoms with a high-resolution microscope onto an intensified charge-coupled device camera. Atoms on doubly occupied sites are removed during the imaging as a consequence of light-assisted collisions (30). We apply a deconvolution algorithm to the images to determine the occupation of every individual lattice site  $n_{\text{det}}$ , which is unity for a single particle of either spin and zero for the case of an empty or doubly occupied site. Our imaging technique allows a reliable determination of the site-resolved occupation, with an estimated imaging fidelity of 97.5(3)% (14, 29).

We directly observed the metal-to-MI transition on a site-resolved level. Single images show a drastic change in the occupation distribution when increasing the interaction,  $U/8\bar{t}$ , at constant atom number (Fig. 1). For the weakest interactions [ $U/8\bar{t} = 1.1(1)$ ], we observed a purely metallic state with a large occupation variance over the entire cloud. The maximum detected value for the variance was 0.25, which is consistent with equal occupation probabilities of all four possible states per lattice site. The occupation decreases gradually for larger distances from the center because of the underlying harmonic confinement. In contrast, for the strongest interactions, [ $U/8\bar{t} = 15.3(7)$ ] we observed a large half-filled MI region containing about 400 atoms (29). The energy gap,  $U$ , suppresses the variance in occupation in the center of the cloud to values below 0.02, with thermal excitations appearing as an increased variance in the occupation at the edge of the cloud.

The underlying harmonic trap causes a spatially varying chemical potential, which can lead to the appearance of different phases within the same atomic cloud. For intermediate interactions [ $U/8\bar{t} = 2.5(1)$  and  $U/8\bar{t} = 3.8(2)$ ], where the chemical potential  $\mu > U$ , we observe a wedding-cake structure, where metallic, MI, and band-insulating (BI) phases coexist. A BI core of doubly occupied sites forms in the center, visible as an extended region of empty sites with low occupation variance. This region is surrounded by a MI with a small number of defects. At the interface of these two phases and at the outer edge of the MI, there is a metallic phase with large occupation variance. For increasing interaction strength, the MI ring broadens owing to the increased energy cost for double occupation. At the same time, the BI region decreases in size, until it disappears entirely for the largest interaction, where  $\mu < U$ . Figure 1C shows radial profiles of the average

Department of Physics, Harvard University, Cambridge, MA 02138, USA.

\*Present address: Max-Planck-Institut für Quantenoptik, 85748 Garching, Germany. †Corresponding author. E-mail: greiner@physics.harvard.edu

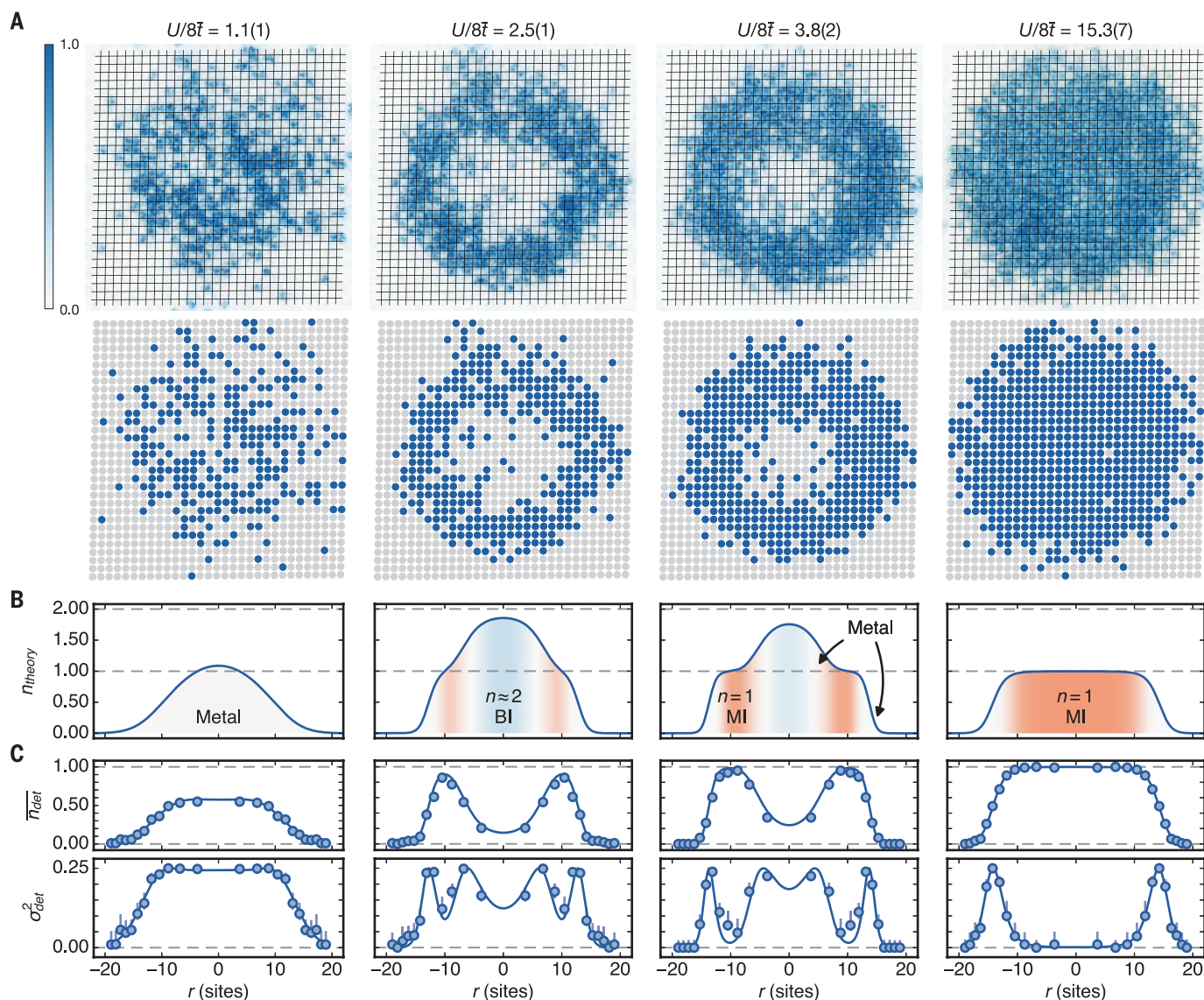


**Fig. 1. Site-resolved images of the fermionic metal-to-MI transition.**

(A) Single experimental images of the atoms in the square lattice are shown for varying interactions  $U/8\bar{t}$ , along with the extracted site occupation. Doublons are detected as empty sites because of light-assisted collisions during imaging. The color bar shows the normalized number of detected photons. (B) Calculated full density profiles for the experimental parameters in (A), obtained by fits to the experimental data. Depending on the interaction, we observe MI, BI, and metallic states. The MI appears for strong interactions as an extended spatial region with filling  $n_{\text{theory}} = 1$ . In the BI, the filling approaches 2. Metallic regions connect the different insulating states, where the filling changes by an integer. (C) By applying azimuthal averages to the corresponding single

detected occupation,  $\bar{n}_{\text{det}}(r)$ , and variance,  $\sigma_{\text{det}}^2(r)$ , obtained from single experimental images by exploiting the symmetry of the trap and taking azimuthal averages over equipotential regions (29).

An essential requirement for a MI state is a temperature well below the energy gap  $k_B T \ll U$ , where  $k_B$  denotes the Boltzmann constant. We perform thermometry of the atomic gas in the lattice by comparing the detected radial occupation and variance profiles obtained from single images to theoretical calculations based on a

second-order high-temperature series expansion of the Fermi-Hubbard model (31). The effect of the harmonic trap is taken into account using a local density approximation, where the chemical potential varies locally (32). The temperature and chemical potential are obtained from a fit to the detected density distribution  $\bar{n}_{\text{det}}(r)$ , and all other parameters are calibrated independently. We find excellent agreement with theory for all interactions and measure temperatures as low as  $k_B T/U = 0.05$  for the largest inter-

images, we obtain radial profiles (mirrored at  $r = 0$ ) for the detected occupation  $\bar{n}_{\text{det}}$  and variance  $\sigma_{\text{det}}^2$ . The variance is strongly reduced in the insulating phases. The radial profiles  $\bar{n}_{\text{det}}(r)$  were fit using a high-temperature series expansion of the single-band Hubbard model, with temperature and chemical potential as free parameters (solid lines). This gives temperatures  $k_B T/U = 1.6(3), 0.22(3), 0.12(2)$ , and  $0.050(7)$  from left to right, which are used for calculating the full density profiles in (B) and correspond to average entropies per particle of  $S/N = 2.2(3), 1.00(8), 0.99(7)$ , and  $1.15(7) k_B$ . The large values of temperature and entropy at  $U/8\bar{t} = 1.1$  may be caused by non-adiabatic loading of the lattice at small interactions. Error bars are computed from a sampled Bernoulli distribution (29).

action, corresponding to an average entropy per particle of  $S/N = 1.15 k_B$ . For weaker interactions, we find values as low as  $S/N = 0.99 k_B$ . When repeating the experiment with the same parameters, we find a shot-to-shot variance in entropy consistent with fit errors (29). The agreement with theory shows that the entire system is well described by a thermally equilibrated state, and the underlying trapping potential is well described by a harmonic trap.

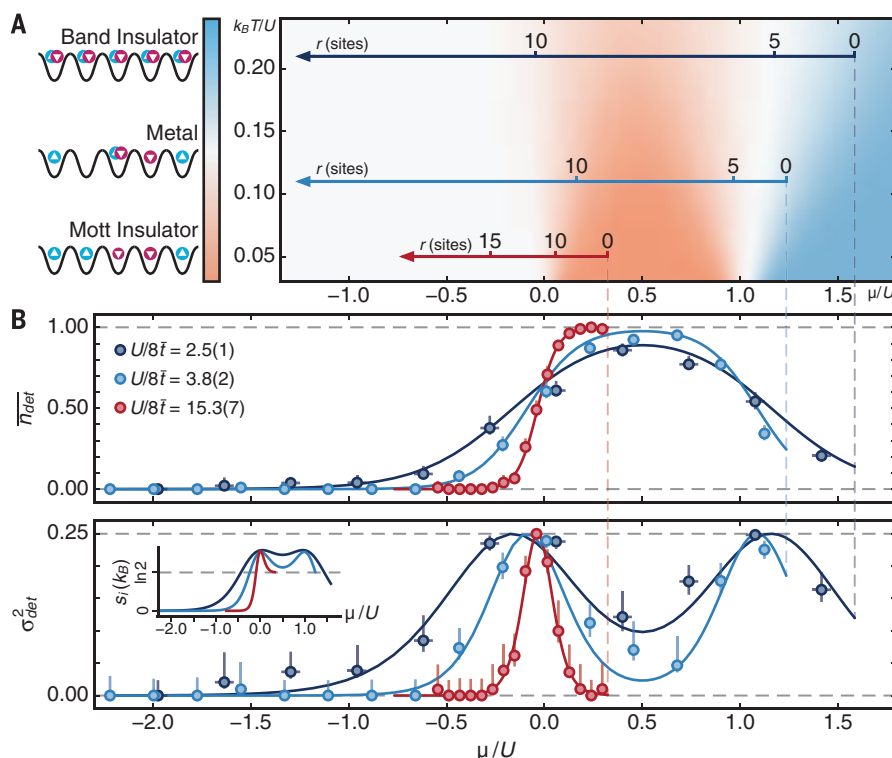


**Fig. 2. Cuts through the 2D Hubbard phase diagram.** (A) Schematic of the  $(\mu/U, k_B T/U)$  phase diagram of the Hubbard model at  $U \gg \bar{t}$ , which is the relevant regime for all three data sets shown. The intensity of the shading reflects the normalized variance of the site occupation, and the colors distinguish between MI and BI regimes. The arrows denote radial cuts through the trap for different interactions corresponding to the profiles shown in (B). (B) Detected site occupation and variance versus chemical potential, obtained from the radial profiles in Fig. 1, with fits as solid lines (29) and error bars as in Fig. 1. The distributions are symmetric around  $\mu = U/2$  (half-filling) from particle-hole symmetry. (Inset, bottom left) Calculated local entropy per site  $s_i$ .

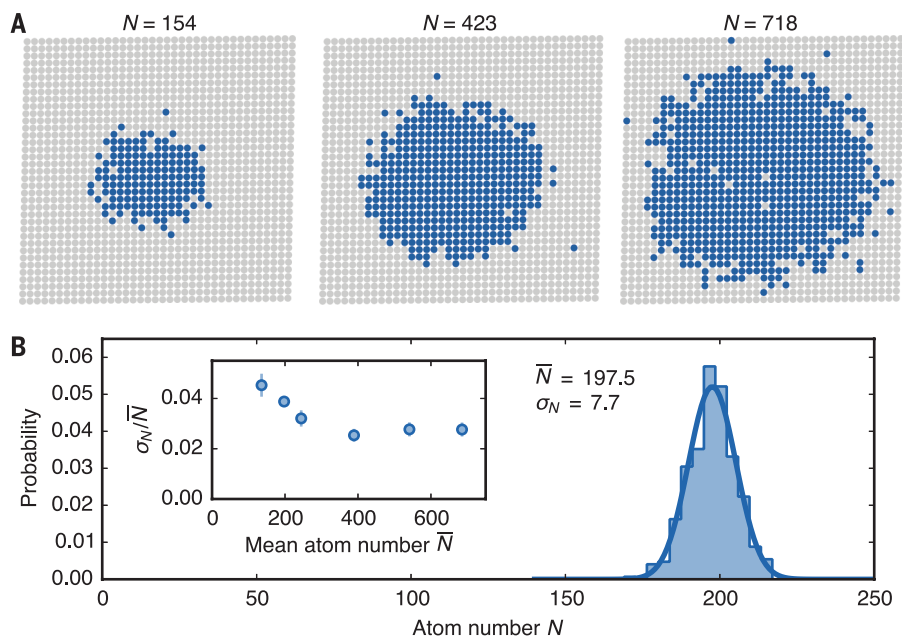


**Fig. 3. Controlling the size of a MI.** (A) Single images of MIs with varying detected atom numbers  $N$  (without doublons) for  $U/8\bar{t} = 15.3(7)$ . (B) Histogram of detected atom numbers after 400 experiment repetitions with the average atom number  $\bar{N}$  and standard deviation  $\sigma_N$  (68% confidence). The solid line shows the Gaussian distribution for the obtained  $\bar{N}$  and  $\sigma_N$ . The inset shows the experimental stability of preparing samples with fixed atom number, characterized by the relative standard deviation for different  $\bar{N}$  obtained from  $\geq 50$  images. Error bars denote the respective standard errors.

In Fig. 2B, we show  $\bar{n}_{\text{det}}$  and  $\sigma_{\text{det}}^2$  as a function of  $\mu/U$ , which corresponds to a scan along a single line in the  $(\mu/U, k_B T/U)$  phase diagram of the Hubbard model at  $t \ll U$ . These data are directly obtained from the respective radial profiles in Fig. 1. The MI is identified by an extended region in  $\mu/U$ , with constant occupation  $\bar{n}_{\text{det}} = 1$  and a strongly reduced variance. Because in this regime the total and detected fillings are approximately equal (see Fig. 1B, right panel), the compressibility in the range just below half-filling ( $\mu < U/2$ ) can be obtained from

$\kappa = \partial n_{\text{det}} / \partial \mu$ , which is small in the MI region. The metallic regions are signaled by an enhanced compressibility, with a peak in the variance distribution. The width of each peak is determined by the temperature and is smallest for the largest interactions, as  $k_B T/U$  decreases for increasing interactions in the experiment.

Two contributions reduce the filling from one particle per site in the MI region: the finite temperature of the gas and the imaging fidelity. We determined a lower bound on the filling by averaging over 50 images, resulting in  $\bar{n}_{\text{det}} =$

96.5(2)%, limited by our finite imaging fidelity of 97.5(3)%. This filling gives an upper bound on the charge entropy (i.e., entropy involving density excitations in the atomic cloud) of  $0.175 k_B$  (29). Because the fermionic particles are in two different spin states, the total entropy also contains a contribution from the spin entropy. From the fitted temperatures we calculate the total entropy per site as a function of  $\mu/U$  for the different interactions (Fig. 2B, inset). In the MI region we find  $s_i = 0.70(1) k_B$ , consistent with  $s_i = k_B \ln 2$ , which corresponds to the entropy of



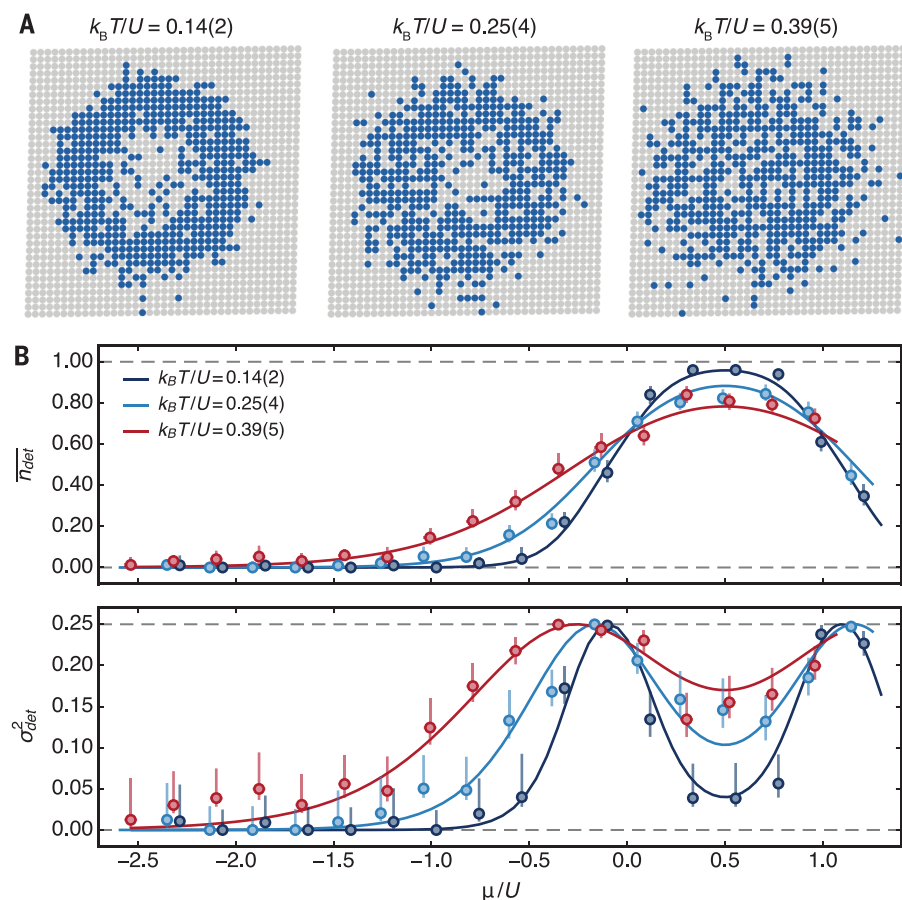


**Fig. 4. Melting a fermionic MI.** (A) Detected site occupations from single images at different temperatures for  $U/8t = 3.8(2)$ . The clouds are heated by holding the atom cloud in a crossed dipole trap before lattice ramp-up. Hold times, from left to right, are 0, 1, and 3 s. (B) Corresponding occupations and variance profiles versus chemical potential, with error bars as in Fig. 1. The dark blue, light blue, and red curves are theory fits used to determine the temperature.

a paramagnetic MI. In the BI region the entropy drops below  $k_B \ln 2$ , as in this case 78(1)% of the lattice sites are occupied with doublons. In the BI, the charge entropy can be estimated from the measured average density of excitations corresponding to sites with one particle. This gives  $0.53(2) k_B$ , in good agreement with the calculated value of  $0.5(1) k_B$  from the theory fit. The variation in local entropy over the atomic cloud indicates that there is not only mass transport, but also efficient transport of entropy over many sites when loading the atoms into the lattice. This entropy transport could be the starting point for generating other low-temperature phases of matter using entropy redistribution or other cooling schemes (33–36).

An accurate experimental study of the low-temperature Hubbard model generally requires large system sizes. By adjusting the evaporation, we experimentally control the size of the MI with detected total atom numbers (without doublons) ranging from  $N = 154$  to  $N = 718$  (Fig. 3). In all cases we find high values for the detected central occupation  $n_{\text{det}} > 0.92$  (28). To investigate the reproducibility, we repeated the same experiment and found that the standard deviation corresponds to  $< 5\%$  of the mean atom number.

Whereas for temperatures  $k_B T \ll U$  a large MI with a sharp occupation distribution appears, the insulator is expected to gradually melt with increasing temperatures and eventually disappear. We experimentally controlled the temperature while keeping the atom number approximately constant by adjusting the evaporation and preparation of the atomic cloud (29). We observed a clear change in the occupation and variance distribution from single images, which is also apparent in the respective distributions as a function of  $\mu/U$  (Fig. 4). For higher temperatures, the occupation distribution broadens significantly, whereas the variance flattens and is only weakly suppressed at the highest detected occupations ( $\mu = U/2$ ). The temperatures determined from theory comparison are in the range  $k_B T/U = 0.14$  to  $0.55$ , which corresponds to entropies of  $S/N = 0.97$  to  $1.58 k_B$ . This shows that temperatures  $k_B T \ll U$  are required for MI states.

For the lowest detected entropy value  $S/N = 0.97 k_B$ , we expect strong antiferromagnetic correlations on nearest-neighbor sites (37–40). This should be detectable in single images by measuring the spin correlation function via spin-sensitive imaging. Additionally, our experiment

is well suited for studying the competition of ferromagnetic and antiferromagnetic domains in the regime of weak lattices and large scattering lengths (41), investigating the phase diagram of polarized samples with repulsive or attractive interactions (42–45), and testing various entropy distribution schemes (33–35).

## REFERENCES AND NOTES

1. L. Balents, *Nature* **464**, 199–208 (2010).
2. P. W. Anderson, *Science* **235**, 1196–1198 (1987).
3. K. D. Nelson, X. Li, D. S. Weiss, *Nat. Phys.* **3**, 556–560 (2007).
4. W. S. Bakr et al., *Science* **329**, 547–550 (2010).
5. J. F. Sherson et al., *Nature* **467**, 68–72 (2010).
6. J. Simon et al., *Nature* **472**, 307–312 (2011).
7. T. Fukuhara et al., *Nat. Phys.* **9**, 235–241 (2013).
8. R. Islam et al., *Nature* **528**, 77–83 (2015).
9. P. M. Preiss et al., *Science* **347**, 1229–1233 (2015).
10. T. Fukuhara et al., *Nature* **502**, 76–79 (2013).
11. P. A. Lee, N. Nagaosa, X.-G. Wen, *Rev. Mod. Phys.* **78**, 17–85 (2006).
12. E. Haller et al., *Nat. Phys.* **11**, 738–742 (2015).
13. L. W. Cheuk et al., *Phys. Rev. Lett.* **114**, 193001 (2015).
14. M. F. Parsons et al., *Phys. Rev. Lett.* **114**, 213002 (2015).
15. G. J. A. Edge et al., *Phys. Rev. A* **92**, 063406 (2015).
16. A. Omran et al., *Phys. Rev. Lett.* **115**, 263001 (2015).
17. R. Jördens, N. Strohmaier, K. Günter, H. Moritz, T. Esslinger, *Nature* **455**, 204–207 (2008).
18. U. Schneider et al., *Science* **322**, 1520–1525 (2008).
19. R. Jördens et al., *Phys. Rev. Lett.* **104**, 180401 (2010).
20. S. Taie, R. Yamazaki, S. Sugawa, Y. Takahashi, *Nat. Phys.* **8**, 825–830 (2012).
21. T. Uehlinger et al., *Phys. Rev. Lett.* **111**, 185307 (2013).
22. P. M. Duarte et al., *Phys. Rev. Lett.* **114**, 070403 (2015).
23. M. Messer et al., *Phys. Rev. Lett.* **115**, 115303 (2015).
24. D. Greif, T. Uehlinger, G. Jotzu, L. Tarruell, T. Esslinger, *Science* **340**, 1307–1310 (2013).
25. R. A. Hart et al., *Nature* **519**, 211–214 (2015).
26. D. Greif, G. Jotzu, M. Messer, R. Desbuquois, T. Esslinger, *Phys. Rev. Lett.* **115**, 260401 (2015).
27. M. Troyer, U.-J. Wiese, *Phys. Rev. Lett.* **94**, 170201 (2005).
28. G. Zürn et al., *Phys. Rev. Lett.* **110**, 135301 (2013).
29. See the supplementary materials on Science Online.
30. M. T. DePue, C. McCormick, S. L. Winoto, S. Oliver, D. S. Weiss, *Phys. Rev. Lett.* **82**, 2262–2265 (1999).
31. J. Oitmaa, C. Hamer, W. Zheng, *Series Expansion Methods for Strongly Interacting Lattice Models* (Cambridge Univ. Press, Cambridge, 2006).
32. V. W. Scarola, L. Pollet, J. Oitmaa, M. Troyer, *Phys. Rev. Lett.* **102**, 135302 (2009).
33. J.-S. Bernier et al., *Phys. Rev. A* **79**, 061601 (2009).
34. T.-L. Ho, Q. Zhou, *Proc. Natl. Acad. Sci. U.S.A.* **106**, 6916–6920 (2009).
35. M. Lubasch, V. Murg, U. Schneider, J. I. Cirac, M.-C. Bañuls, *Phys. Rev. Lett.* **107**, 165301 (2011).
36. W. S. Bakr et al., *Nature* **480**, 500–503 (2011).
37. S. Fuchs et al., *Phys. Rev. Lett.* **106**, 030401 (2011).
38. B. Tang, T. Paiva, E. Khatami, M. Rigol, *Phys. Rev. Lett.* **109**, 205301 (2012).
39. J. P. F. LeBlanc, E. Gull, *Phys. Rev. B* **88**, 155108 (2013).
40. J. Imriška, E. Gull, M. Troyer, Thermodynamics of the Hubbard model on stacked honeycomb and square lattices, <http://arxiv.org/abs/1509.08919> (2015).
41. P. N. Ma, S. Piliati, M. Troyer, X. Dai, *Nat. Phys.* **8**, 601–605 (2012).
42. M. Snoek, I. Titvinidze, C. Töke, K. Byczuk, W. Hofstetter, *New J. Phys.* **10**, 093008 (2008).
43. B. Wunsch, L. Fritz, N. T. Zinner, E. Manousakis, E. Demler, *Phys. Rev. A* **81**, 013616 (2010).
44. A. Koetsier, F. van Lier, H. T. C. Stoof, *Phys. Rev. A* **81**, 023628 (2010).
45. J. Gukelberger, S. Lienert, E. Kozik, L. Pollet, M. Troyer, Fulde-Ferrell-Larkin-Ovchinnikov pairing as leading instability on the square lattice, <http://arxiv.org/abs/1509.05050> (2015).

## ACKNOWLEDGMENTS

We acknowledge insightful discussions with I. Bloch, S. Dickerson, M. Endres, G. Jotzu, and A. Kaufman. We acknowledge support

from the Army Research Office Defense Advanced Research Projects Agency Optical Lattice Emulator, the Air Force Office of Scientific Research, the Multi University Research Initiative, the Office of Naval Research Defense University Research Instrumentation Program, and NSF. D.G. acknowledges support from the Harvard Quantum Optics Center and the Swiss National Foundation. M.P., A.M. and C.C. acknowledge support from the NSF

Graduate Research Fellowship Program. The authors declare no competing financial interests.

# SUPPLEMENTARY MATERIALS

www.sciencemag.org/content/351/6276/953/suppl/DC1  
Supplementary Text

Figs. S1 to S7  
Table S1  
Reference (46)

18 November 2015; accepted 27 January 2016  
10.1126/science.aad9041

## THIN FILMS

# Superlubricity of graphene nanoribbons on gold surfaces

Shigeki Kawai,<sup>1,2,\*</sup> Andrea Benassi,<sup>3,4,\*</sup> Enrico Gnecco,<sup>5,6</sup> Hajo Söde,<sup>3</sup> Rémy Pawlak,<sup>1</sup> Xinliang Feng,<sup>7</sup> Klaus Müllen,<sup>8</sup> Daniele Passerone,<sup>3</sup> Carlo A. Pignedoli,<sup>3</sup> Pascal Ruffieux,<sup>3</sup> Roman Fasel,<sup>3,9</sup> Ernst Meyer<sup>1</sup>

The state of vanishing friction known as superlubricity has important applications for energy saving and increasing the lifetime of devices. Superlubricity, as detected with atomic force microscopy, appears when sliding large graphite flakes or gold nanoclusters across surfaces, for example. However, the origin of the behavior is poorly understood because of the lack of a controllable nanocontact. We demonstrated the superlubricity of graphene nanoribbons when sliding on gold with a joint experimental and computational approach. The atomically well-defined contact allows us to trace the origin of superlubricity, unraveling the role played by ribbon size and elasticity, as well as by surface reconstruction. Our results pave the way to the scale-up of superlubricity and thus to the realization of frictionless coatings.

Graphene offers distinctive properties as a solid lubricant (*1*) and has the potential to be used as an ultrathin coating material on surfaces, almost suppressing energy consumption in mechanical components. The interpretation of such superlubric behavior is based on the premise that (2–5) (i) the high lateral stiffness of graphene makes a commensurate contact with most solid surfaces nearly

impossible, and (ii) combined with the weak interaction with most materials, incommensurability leads to a state of ultralow friction when graphene slides over a different material. To substantiate this hypothesis and establish a connection with the tribological properties observed on macro- and mesoscales, it is highly desirable to measure the mechanical response of a graphene flake down to the nanometer level. In such mea-

surements, one has to ensure that both of the contacting surfaces are atomically well defined, that their common interface is free from contaminants, and that the ultralow forces accompanying the sliding motion can be distinguished from the background noise. Whereas clean atomically flat surfaces as substrates can reliably be obtained in ultrahigh vacuum (UHV), atomically defined graphene systems as sliding objects are rarely prepared. Carbon nanotubes have exceptional superlubric properties up to a length scale

<sup>1</sup>Department of Physics, University of Basel, Klingelbergstrasse 82, CH-4056 Basel, Switzerland. <sup>2</sup>PRESTO (Precursory Research for Embryonic Science and Technology), Japan Science and Technology Agency, 4-1-8 Honcho, Kawaguchi, Saitama 332-0012, Japan. <sup>3</sup>nanotech@surfaces Laboratory, Empa, Swiss Federal Laboratories for Materials Science and Technology, Überlandstrasse 129, 8600 Dübendorf, Switzerland. <sup>4</sup>Institute for Materials Science and Max Bergmann Center of Biomaterials, Technische Universität Dresden, 01062 Dresden, Germany. <sup>5</sup>Instituto Madrileño de Estudios Avanzados en Nanociencia, 28049 Madrid, Spain. <sup>6</sup>Otto Schott Institute of Materials Research, Friedrich Schiller University Jena, 07743 Jena, Germany. <sup>7</sup>Department of Chemistry and Food Chemistry, Center for Advancing Electronics Dresden, Technische Universität Dresden, 01062 Dresden, Germany. <sup>8</sup>Max Planck Institute for Polymer Research, 55124 Mainz, Germany. <sup>9</sup>Department of Chemistry and Biochemistry, University of Bern, Freiestrasse 3, 3012 Bern, Switzerland.

\*Corresponding author. E-mail: shigeki.kawai@unibas.ch (S.K.); andrea.benassi@nano.tu-dresden.de (A.B.) †These authors contributed equally to this work.

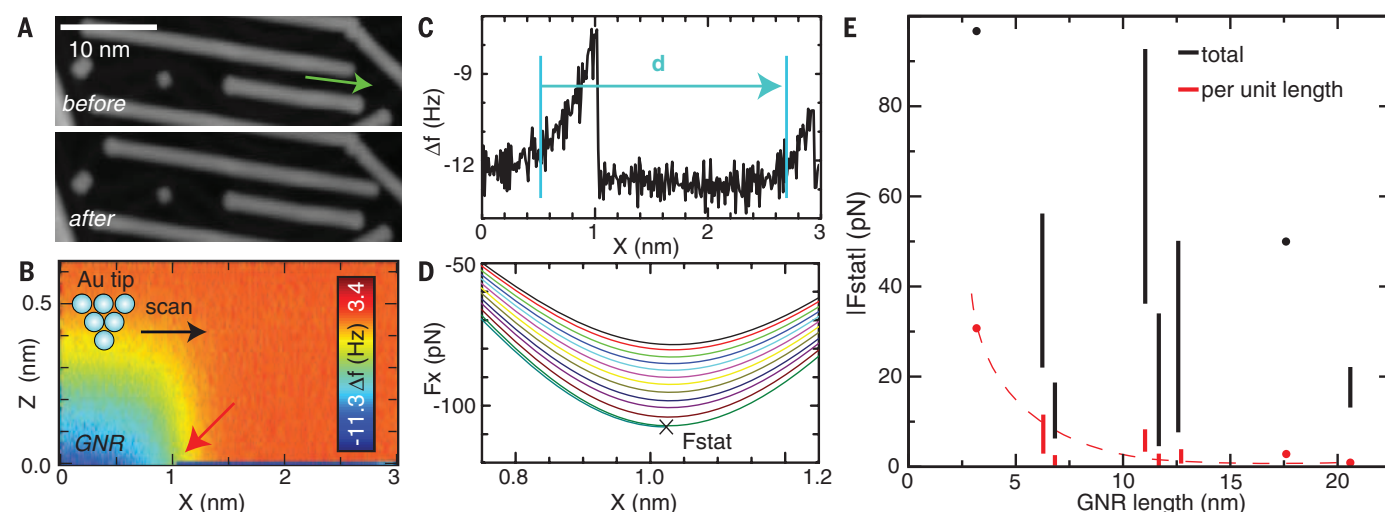


**Fig. 1. Static friction force measurement.** (A) STM topographies of GNRs on Au(111) before and after a tip-induced lateral manipulation (the green arrow indicates the sliding direction). (B) 2D  $\Delta f$  map along the longitudinal axis of the manipulated GNR. (C) Distance dependence of  $\Delta f$  before, during, and after the GNR displacement. (D) Calculated lateral force. The cross symbol corresponding to the red arrow in (B) shows the position at which the GNR starts moving

and the corresponding value of the static friction force  $F_{stat}$ . (E) The absolute value of  $F_{stat}$  as a function of the GNR length (black) and  $F_{stat}$  per unit length (red). Dots correspond to single measurements, whereas bars connect the largest and the smallest values measured while manipulating the same ribbon on different surface regions. Measurement parameters: tunneling current  $I = 2$  pA, bias voltage  $V = -200$  mV (A); oscillation amplitude  $A = 34$  pm [(B) to (D)].

## Site-resolved imaging of a fermionic Mott insulator

Daniel Greif, Maxwell F. Parsons, Anton Mazurenko, Christie S. Chiu, Sebastian Blatt, Florian Huber, Geoffrey Ji and Markus Greiner

*Science* **351** (6276), 953-957.  
DOI: 10.1126/science.aad9041

### Watching fermions transition on site

Optical lattices are a promising platform for simulating the many-body physics that occurs in solids. In lattices filled with cold bosonic atoms, "quantum microscopy" makes it possible to watch quantum phase transitions as they unravel. Greif *et al.* bring a similar capability to lattices filled with fermions, which are trickier to cool but are a closer match to electrons in a solid. Tuning the interaction between the  $^6\text{Li}$  atoms allowed for the observation of transitions from a metallic phase to a band insulator and then to an interaction-dominated Mott insulator phase.

*Science*, this issue p. 953

#### ARTICLE TOOLS

<http://science.sciencemag.org/content/351/6276/953>

#### SUPPLEMENTARY MATERIALS

<http://science.sciencemag.org/content/suppl/2016/02/24/351.6276.953.DC1>

#### REFERENCES

This article cites 42 articles, 5 of which you can access for free  
<http://science.sciencemag.org/content/351/6276/953#BIBL>

#### PERMISSIONS

<http://www.sciencemag.org/help/reprints-and-permissions>

Use of this article is subject to the [Terms of Service](#)